AIAA JOURNAL
Vol. 43, No. 11, November 2005

Turbulent Characteristics of a Transverse Supersonic Jet in a Subsonic Compressible Crossflow

Steven J. Beresh,* John F. Henfling,† Rocky J. Erven,‡ and Russell W. Spillers§
Sandia National Laboratories, Albuquerque, New Mexico 87185

Fluctuating velocity fields have been determined from particle image velocimetry data acquired in the far field of the interaction generated by an overexpanded axisymmetric supersonic jet exhausting transversely from a flat plate into a subsonic compressible crossflow. Peak magnitudes of the turbulent stresses were found to be larger and located farther from the wall for greater values of the jet-to-freestream dynamic pressure ratio J while the crossflow Mach number M_∞ remained constant. These stress magnitudes diminish with downstream distance as their peak location moves farther from the wall. The vertical positions of the peak normal stresses and shear stress inflection point coincide with the maximum mean streamwise velocity deficit induced by the jet. Similarity in the turbulent stress profiles was demonstrated for constant J at two transonic M_∞, but not at two lower M_∞. Instantaneous realizations of the velocity fluctuation fields reveal large-scale eddies whose mean diameter is greater for larger J and decreases with downstream distance. The integral length scale calculated from profiles of the correlation coefficient instead shows an increasing downstream trend along with a larger magnitude; the discrepancy between the two length scales results from a low-pass filter effect of the correlation coefficient.

Introduction

SUPERSONIC jets used for attitude or roll control on atmospheric flight vehicles produce exhaust plumes that, upon encountering a crossflowing freestream, are reoriented to travel downstream where they can interact with aft aerodynamic control surfaces.[1–6] This jet/fin interaction is fundamentally defined by the jet-in-crossflow interaction between the exiting jet and the freestream, which is sketched in Fig. 1 based on the observations of past studies.[7–13] The far field of the interaction is dominated by the presence of a counter-rotating vortex pair, induced as the jet is turned over and realigned by its encounter with the freestream. Additional turbulent structures include horseshoe vortices generated by separation immediately upstream of the jet as it exits the nozzle and wake vortices shed behind the jet in a fashion similar to a vortex street emanating from a cylinder in crossflow. The instantaneous appearance of the decaying jet plume and the counter-rotating vortex pair does not possess the pleasing symmetry shown in the sketch, but, rather, have superimposed upon them eddies associated with turbulent mixing between the jet and the freestream.

Because the jet-in-crossflow interaction is an inherently unsteady flow, accurate computational prediction of the mean flowfield behavior generally requires knowledge of the instantaneous turbulent properties, which can come only from experimental measurements. Although the jet in crossflow is one of the classic problems of fluid mechanics, the necessary data for aerodynamic applications are lacking. Experiments of jet-in-crossflow interactions are common at low speeds, but such work is less plentiful in the compressible regime and rarer still if turbulent quantities are measured. This absence largely is owing to the difficulty of acquiring such data at high velocities; nevertheless, the known literature is not entirely devoid of such efforts. Planar laser diagnostics have been used to measure the instantaneous interface shape of the vortex pair and the scalar mixing of a supersonic jet interaction.[14,15] Hot-film anemometry has been employed to measure the turbulent stresses and associated turbulent properties in an angled jet in supersonic crossflow.[16,17] Similar data have been acquired in a sonic jet interaction using laser Doppler velocimetry.[18]

The present work aims to add to this knowledge base by experimentally examining the interaction generated by a supersonic jet exhausting transversely from a flat plate into a subsonic compressible crossflow. Two-dimensional particle image velocimetry (PIV) was conducted in the centerline streamwise plane of the far field of the jet-in-crossflow interaction to determine the streamwise and vertical velocity components, from which turbulent properties can be derived. Data were collected for varied flowfield conditions to examine the impact of altering the jet-to-freestream dynamic pressure ratio and the freestream Mach number, which previously have been identified as key similarity parameters.[7,19–22] An earlier publication examined the mean data derived from these experiments to measure the trajectory of the jet and the associated vortex pair.[23] The current document analyzes the same data set to ascertain the turbulent stresses of the interaction and the characteristic large-scale turbulent structures found in the far field. Although these turbulent quantities are incomplete in that they do not include the third velocity component or the density fluctuations necessary for Favre averaging, they do provide important information for the validation of computational simulations and the evolution of their underlying physical models by providing greater detail than that revealed solely by time-integrated methods.

Experimental Apparatus

An abbreviated description of the experimental implementation is provided herein; a more detailed treatment can be found in Ref. 23.

Trisonic Wind Tunnel

All experiments were performed in the Sandia National Laboratories Trisonic Wind Tunnel (TWT) in its solid-wall transonic configuration, which imposes a subsonic Mach-number limitation. The TWT is a blowdown-to-atmosphere facility using air as the test gas through a 305×305 mm^2 (12×12 in.^{2}) rectangular test section. The use of solid walls serves both to supply a flat plate from which the jet will issue and to provide computationally tractable boundary conditions for comparison of experimental data and numerical simulations.

Presented as Paper 2004-2341 at the AIAA 34th Fluid Dynamics Conference, Portland, OR, 28 June–1 July 2004; received 12 November 2004; revision received 10 May 2005; accepted for publication 3 June 2005.

*Principal Member of the Technical Staff, P.O. Box 5800, Mailstop 0834, Engineering Sciences Center; sjberes@sandia.gov. Senior Member AIAA.
†Distinguished Technologist, Engineering Sciences Center. Member AIAA.
‡Principal Technologist, Engineering Sciences Center.
§Technologist, Engineering Sciences Center.

Supersonic Jet Hardware

The jet exhausted from a conical nozzle with a design Mach number of 3.73, an expansion half-angle of 15 deg, and an exit diameter of 9.53 mm (0.375 in.). It was supplied by nitrogen at a maximum pressure of 14 MPa (2000 psia) and instrumented for stagnation pressure and temperature measurements. The nozzle was mounted along the centerline of the top wall of the test section, which served as the flat plate from which it transversely exhausted. Side-wall windows are positioned downstream of the jet for viewing the far field of the interaction; a window in the floor of the test section allows introduction of the laser sheet. The relative position of the jet and windows within the test section is sketched in Fig. 2, which additionally shows the laser sheet for the PIV measurements and the side-wall pressure taps.

PIV System

PIV measurements used in the current study are two-dimensional, acquired with the laser sheet aligned in the streamwise direction of the wind tunnel positioned downstream of the jet nozzle on the test section centerline, as shown in Fig. 2. The plane in which the laser sheet lies passes through the centerline axis of the jet nozzle. The coordinate system is chosen such that the u component lies in the streamwise direction and the v component is in the vertical direction, positive away from the top wall. The origin is located at the center point of the jet nozzle exit plane.

The light source of the system is a pair of frequency-doubled Nd:YAG lasers (Coherent Infinity 40-100) with the beams combined and formed into coplanar sheets beneath the wind tunnel and directed into the test section. The sheet thickness is 1.2 mm (0.048 in.), and the pulse separation time is 2.375 ± 0.005 μs. Scattered light is collected by a 2048×2048 pixel frame-straddling charge-coupled-device camera (Redlake MegaPlus ES4.0/E) equipped with a 105-mm lens (Nikon Micro-Nikkor) operating at f/4. The field of view measures approximately 160×160 mm^2 (6.2×6.2 in.^{2}).

The flowfield was surveyed using two separate imaging regions, as indicated in Fig. 2, to measure a greater streamwise distance of the interaction; each region was captured in a separate set of wind-tunnel runs. The farthest upstream edge of the combined imaging region was constrained by the side-wall window through which the camera looked, whereas the farthest downstream edge was limited by the laser-sheet projection.

The TWT is seeded by a thermal smoke generator (Corona Vi-Count 5000) that produces a large quantity of particles 0.2–0.3 μm in diameter, which are forced through a duct into the TWT's stagnation chamber and distributed upstream of the flow conditioning section. The jet itself remains unseeded. Although this creates a measurement bias near the jet exit because of selective flow sampling, data acquired further downstream are not subject to such a difficulty because turbulent mixing entrains particles from the freestream and spreads them throughout the interaction once in the far field. The particles are sufficiently small that they rapidly attain the local velocity once they have been redistributed.[24,25]

PIV data have been processed using Integrated Design Tools, Inc.,'s ProVision 2.02 software. Vectors are produced using a 64×64 pixel interrogation window with a 50% overlap, yielding a 5.0×5.0 mm^2 (0.20×0.20 in.^{2}) spatial resolution. A streamwise window offset is established between the two exposures corresponding to the freestream convection distance. Resulting vector fields are validated based upon signal-to-noise and nearest-neighbor criteria.

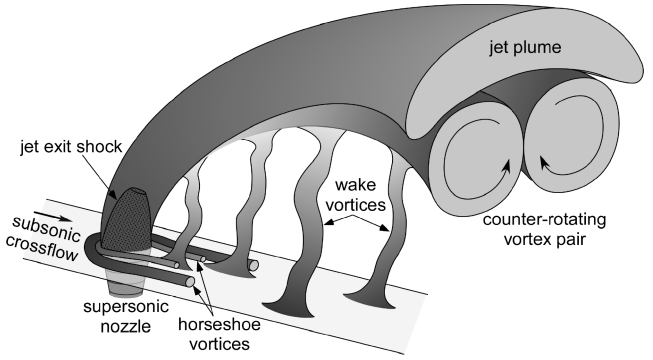

Fig. 1 Sketch of the common features of a jet-in-crossflow interaction.

Experimental Conditions

The primary freestream Mach number is $M_\infty = 0.8$ with a wind-tunnel stagnation pressure $P_0 = 154$ kPa (22.4 psia), which yields

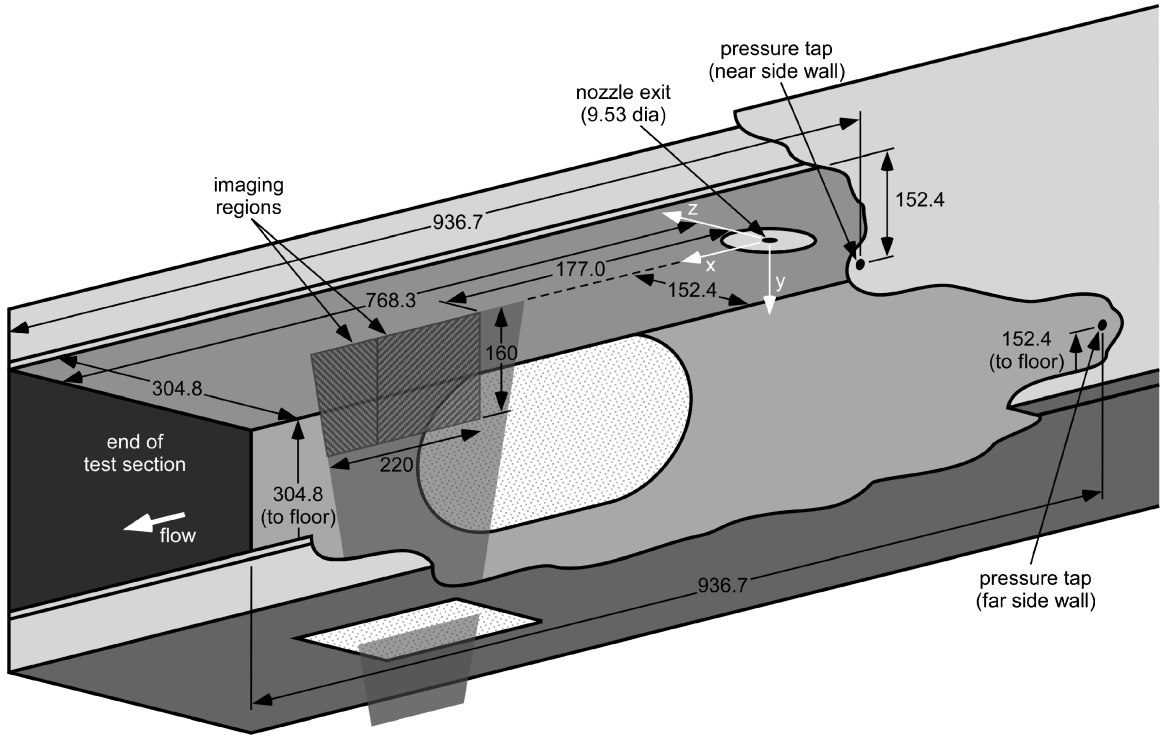

Fig. 2 Schematic of the jet-in-crossflow configuration in the TWT for PIV measurements, looking in the downstream direction. Flow is from right to left. All dimensions are in millimeters. The sketch is not to scale.

a test-section static pressure $p_w = 101$ kPa (14.7 psia) and a wind-tunnel unit Reynolds number of 20×10^6 m^{-1} (6×10^6 ft^{-1}). The nominal stagnation pressure for the Mach 3.73 jet is $P_{0j} = 4.96$ MPa (720 psia), providing a perfectly expanded jet exit pressure of $p_e = 47.1$ kPa (6.84 psia). These conditions combine to produce a nominal jet-to-freestream dynamic pressure ratio $J = 10.2$. Additional cases span a range of J values while maintaining a constant $M_\infty = 0.8$, or span a range of subsonic values of M_∞ while maintaining a constant $J = 10.2$. Table 1 lists the conditions for the seven cases studied herein. All cases were chosen such that the freestream static pressure $p_w = 101$ kPa (14.7 psia); therefore, the jet was always overexpanded. This wall pressure was measured from the mean of two static-pressure taps located on the wind-tunnel side walls 168 mm upstream of the jet nozzle centerline, as seen in Fig. 2. M_∞ and the velocity reference U_∞ were calculated isentropically from the ratio p_w/P_0 and the stagnation temperature T_0. The choice of M_∞ and J must keep within the subsonic restrictions imposed by the tunnel blockage issues inevitable with the solid-wall transonic test section.

The gas supply for the jet is unheated, and so the jet stagnation temperature T_{0j} varied from 296 to 307 K (533 to 553°R), depending on the laboratory ambient conditions. The wind-tunnel air supply is heated in the storage tanks, but is not temperature-controlled subsequent to this; therefore, the freestream stagnation temperature T_0 also is subject to slight variation and fluctuated from 324 to 329 K (582 to 591°R).

Table 1 Experimental conditions for the jet and wind tunnel

Case	J	M_∞	P_0, kPa	P_{0j}, MPa	U_∞, m/s
1	10.2	0.80	154	4.97	286
2	16.7	0.80	154	8.14	286
3	5.6	0.80	154	2.76	286
4	2.8	0.80	154	1.36	286
5	10.2	0.70	141	3.82	251
6	10.2	0.60	129	2.79	215
7	10.2	0.50	120	1.96	181

The 99%-velocity boundary-layer thickness has been determined from the present PIV data on the wind-tunnel top wall in the undisturbed test section, in which the jet nozzle has been replaced by a blank to preserve the flat wall. At the center of the upstream PIV imaging region, which is 254 mm downstream of the jet nozzle centerline, the data yield a value of 14.8 ± 0.4 mm ($1.53 \pm 0.1\, d_j$). Optical access precludes boundary-layer measurements immediately upstream of the jet nozzle.

The trapezoidal PIV imaging region stretches from 176 to 440 mm downstream of the jet nozzle centerline, or 18.5 to 46.2 jet diameters d_j, although the inclined laser sheet limits the horizontal edge to 400 mm ($42.0\, d_j$) downstream at the edge furthest from the wall. For the nominal flow conditions (case 1 in Table 1), 15 wind-tunnel runs totaling 3015 image pairs were collected at the upstream imaging region and nine wind-tunnel runs totaling 1809 image pairs at the downstream position. For each of the other six cases, five wind-tunnel runs totaling 1005 image pairs were conducted for each camera position.

Results and Discussion

Velocity Fields

All valid vectors were averaged into a mean velocity field for each of the seven cases. The streamwise component u and the vertical component v for the nominal flow conditions of $J = 10.2$ and $M_\infty = 0.8$ are shown in Figs. 3a and 3b, respectively, which are reproduced from Ref. 23. Distances are normalized to the jet exit

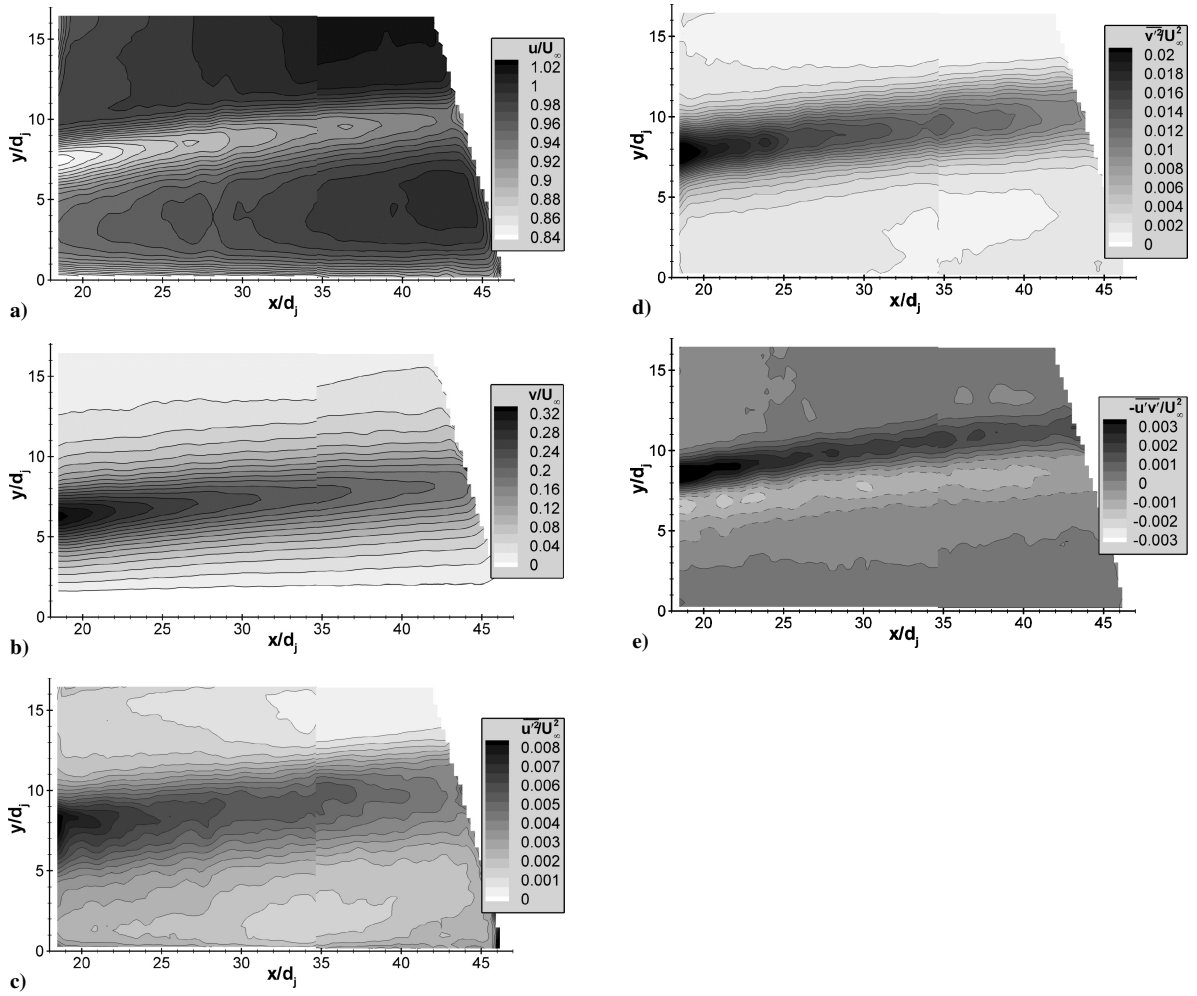

Fig. 3 Velocity data for the jet-in-crossflow interaction at $J = 10.2$ and $M_\infty = 0.8$: a) mean streamwise velocity component (from Ref. 23), b) mean vertical velocity component (from Ref. 23), c) streamwise turbulent stress, d) vertical turbulent stress, and e) turbulent shear stress.

diameter d_j and velocities to U_∞. In the interest of brevity, the velocity fields are not shown for the other six cases but can be found elsewhere.[23]

The streamwise velocity component in Fig. 3a shows that the position of the jet can be tracked by its impedance of the crossflow, while Fig. 3b shows that the position of the counter-rotating vortex pair is evident because of the induced vertical velocity. The position of the maximum deficit in u does not coincide with the maximum in v, indicating that the vortex pair is closer to the wall than the jet itself. The decay of the jet and vortex strength with downstream distance is apparent from the decrease in the deficit in u and the magnitude in v as both move farther from the wall. The perceived reduction in velocity along the inclined downstream edge of the measurement region is an artifact of proximity to the edge of the laser sheet. The gradual streamwise increase in the freestream value of u in Fig. 3a occurs because the wind-tunnel test section has a constant cross-sectional area; hence, the local Mach number increases as the wall boundary-layer growth and the jet penetration increase the tunnel blockage. Curiously, $u/U_\infty = 1$ occurs near the middle of the PIV imaging region despite its downstream distance from the wall pressure taps at which M_∞ and U_∞ are calculated. This suggests a measurement bias estimated as 2–3% of U_∞, which is believed to result from flow nonuniformities near the test section inlet.

Turbulent velocities u' and v' are easily found by subtracting the mean velocity fields from each instantaneous vector field, from which the turbulent stresses $\overline{u'^2}$, $\overline{v'^2}$, and $-\overline{u'v'}$ can be computed. These are shown in Figs. 3c, 3d, and 3e, respectively, for the nominal case of $J = 10.2$ and $M_\infty = 0.8$. The maximum values in $\overline{u'^2}$ and $\overline{v'^2}$ appear to coincide with the trajectory of the jet found from the maximum streamwise velocity deficit. The turbulent shear stress $-\overline{u'v'}$ shows the dual-banded appearance from the positive and negative shearing that is characteristic of such a mixing layer, with the inflection point also apparently located at the maximum deficit in u. As with the mean measurements, the stress magnitudes decay with downstream distance while their peak locations move further from the wall. These observations will be discussed in greater detail next.

The turbulent stresses in Figs. 3c, 3d, and 3e are noticeably noisier than the mean velocities in Figs. 3a and 3b because of poorer statistical convergence for these measurements. Whereas mean measurement uncertainty is dominated by calibration error, turbulent stress uncertainties are more strongly subject to convergence error. Furthermore, the streamwise turbulent stress in Fig. 3c exhibits greater noise than the vertical turbulent stress in Fig. 3d. This is because the magnitude of $\overline{u'^2}$ is less than that of $\overline{v'^2}$ and reduces the measurement signal-to-noise ratio.

Turbulent Stress Profiles

The measurements shown in Fig. 3, and those like them for the other six cases, can be viewed in a more quantitative format by extracting specific vertical lines of data at 200, 250, 300, 350, and 400 mm downstream of the jet nozzle centerline (21.0, 26.2, 31.5, 36.7, and 42.0 d_j downstream). Profiles of the two mean velocity components can be found in Ref. 23, whereas the turbulent stress profiles are shown in Figs. 4 and 5 for those cases where M_∞ is constant and J is constant, respectively.

From the mean velocity data in Ref. 23, it was observed that when M_∞ is held constant the maximum deficit in u and the maximum magnitude of v increase with larger J, both of which also decay with downstream distance. The penetration of the jet, evident in the vertical position of these maxima, is greater for larger J and continually increases with downstream distance. The width of the peak in these profiles is greater for larger J as well and increases with downstream distance, indicating that the size and strength of the jet and vortices are greater for larger J and that they grow larger while traveling downstream. The behavior with constant J and varying M_∞ is more complex, wherein similarity in the mean velocity field was observed for $M_\infty = 0.8$ and 0.7 but not for $M_\infty = 0.6$ and 0.5. In the latter two cases, an interaction between the jet and the boundary layer apparently occurs, and no clear distinction between the jet and its wake can be made as in the other cases.

An examination of the turbulent stress profiles in Figs. 4 and 5 reveals similar trends. At larger J while M_∞ is constant, the maximum magnitude of both $\overline{u'^2}/U_\infty^2$ and $\overline{v'^2}/U_\infty^2$ is greater, as is the width of the peak. The peaks of $-\overline{u'v'}/U_\infty^2$, both positive and negative, are greater for larger J as well. The vertical positions of these peak stresses increase with J and with downstream distance, while their magnitudes diminish with downstream distance. In Fig. 5, similarity can be observed to within the measurement uncertainty for $M_\infty = 0.8$ and 0.7 but not for $M_\infty = 0.6$ and 0.5, just as for the mean data. Taken as a whole, these measurements indicate that the turbulent stresses scale with the strength and position of the jet.

The noise caused by the limited statistical convergence of the turbulent stress profiles plotted in Figs. 4 and 5 is clearer than was visible in the contour plots of Fig. 3. Greater noise is seen for $\overline{u'^2}/U_\infty^2$ and $-\overline{u'v'}/U_\infty^2$ than for $\overline{v'^2}/U_\infty^2$ owing to the larger signal-to-noise ratio for the latter value. The noise also is less for the $J = 10.2$ and $M_\infty = 0.8$ condition, for which a greater quantity of images was acquired.

Data uncertainties were found using the $J = 10.2$ and $M_\infty = 0.8$ case, in which the larger volume of data spanned several days and therefore used multiple PIV calibrations. Total uncertainty was found by comparing data acquired using different calibrations, while convergence uncertainty was found from multiple wind-tunnel runs within the same calibration. Calibration error could be isolated by subtracting the convergence uncertainty from the total uncertainty in a rss fashion. For every case except $J = 10.2$ and $M_\infty = 0.8$, a single calibration was used, and hence the calibration uncertainty is fixed, whereas the convergence uncertainty reduces with the quantity of data:

$$\sigma_{\text{total}}^2 = \sigma_{\text{calibration}}^2 + \sigma_{\text{convergence}}^2 \Big/ \sqrt{N}$$

Here N is the number of wind-tunnel runs for a given case, which is five in most cases. This approach was used to derive the error bars found in Figs. 4 and 5, defined as 95% confidence intervals, which are conservative for $J = 10.2$ and $M_\infty = 0.8$ because the data set for this condition is larger. The typical uncertainty in J is ± 0.1 and in M_∞ is ± 0.002, again determined as 95% confidence intervals; these run-to-run variations in the flowfield parameters are partly responsible for the convergence uncertainties.

The horizontal lines superposed on the turbulent stress profiles in Fig. 4 indicate the vertical position of the maximum velocity deficit in u, determined from the profiles found in Ref. 23. Such maxima are not included for Fig. 5 because no distinct peak is found for the deficit in u for the $M_\infty = 0.6$ and 0.5 cases and the similarity between $M_\infty = 0.8$ and 0.7 makes these cases redundant with Fig. 4. Figure 4a shows that this maximum in the u deficit occurs very near the maximum in $\overline{u'^2}/U_\infty^2$, although the noise from convergence error hampers this comparison, particularly for the $J = 16.7$ case. The convergence error is markedly less in Fig. 4b, where it is clear that the peak in $\overline{v'^2}/U_\infty^2$ coincides with the peak in the u deficit and not the peak of v, the latter of which lies beneath the former.[23] Figure 4c shows that the inflection point of the $-\overline{u'v'}/U_\infty^2$ profiles occurs at the maximum u deficit.

The behavior of the turbulent stress profiles for the $M_\infty = 0.6$ and 0.5 cases differs from the others. The profiles of $\overline{u'^2}/U_\infty^2$, although noisier because of the lower measurement signal-to-noise ratio from the lower U_∞, maintain a relatively constant value from the jet to the wall, consistent with the behavior of the u deficit.[23] The largest value of $\overline{u'^2}/U_\infty^2$ is similar to that for the $M_\infty = 0.8$ and 0.7 cases; the largest value of $\overline{v'^2}/U_\infty^2$, however, is less than that for $M_\infty = 0.8$ and 0.7, suggesting that the turbulence is more isotropic for the $M_\infty = 0.6$ and 0.5 cases. In Fig. 5c, two inflection points in the $-\overline{u'v'}/U_\infty^2$ profile are seen for $M_\infty = 0.6$ and 0.5, rather than the expected single occurrence. This is most evident farther upstream.

Because the w component of velocity was not measured, it is not possible to compute the turbulent kinetic energy of the flowfield. Nevertheless, it is a plausible inference that the peak of $\overline{w'^2}/U_\infty^2$ will occur at the same vertical location as the peaks of $\overline{u'^2}/U_\infty^2$ and $\overline{v'^2}/U_\infty^2$; if that is the case, the peak of the turbulent kinetic energy coincides with the maximum u deficit and hence the position of the decaying jet. The anisotropy, on the other hand, can be computed for one of its three components. Figure 6 shows A_{xy}, defined here

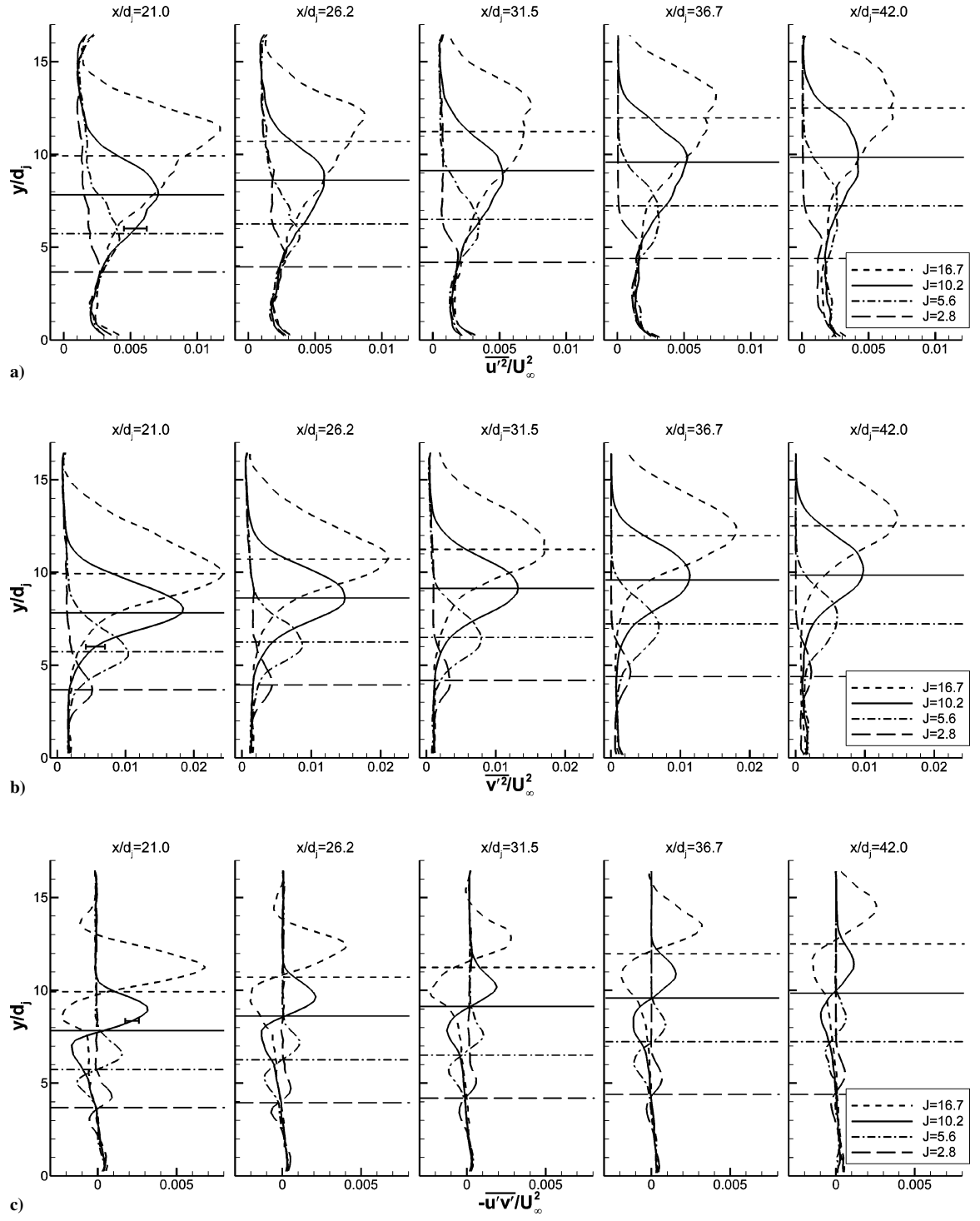

Fig. 4 Turbulent stress data extracted from vector fields at five locations downstream of the jet nozzle centerline for varying values of J while $M_\infty = 0.8$: a) streamwise turbulent stress, b) vertical turbulent stress, and c) turbulent shear stress. The horizontal lines indicate the vertical location of the maximum deficit in u.

as $\overline{v'^2}/\overline{u'^2}$, for $x/d_j = 21.0$. Other downstream positions are similar, save that the width and position of the peak adjust to the growth and increasing penetration of the jet. No reduction in the maximum value of A_{xy} with downstream distance is observed to within the measurement uncertainty. It also is shown that the peak anisotropy is reasonably constant at about 2.5, except for $J = 2.8$, where the jet is weak, and the $M_\infty = 0.6$ and 0.5 cases where variant flow behavior has already been established.

Instantaneous Velocity Fields

Instantaneous realizations of the velocity fluctuation data also can be analyzed for insight into the coherent structures found as the jet mixes with the freestream. A representative vector field of the velocity fluctuations overlaid upon the derived vorticity field is shown in Fig. 7a for $J = 10.2$ and $M_\infty = 0.8$. Only the upstream imaging window is shown, as data acquired from the downstream window were obtained at a different time and hence are uncorrelated with it. The most prominent feature of the vector field is eddies of both positive and negative vorticity that are instantaneously present in the mixing region. These structures can be seen to be generally elliptical in nature with varied degrees of stretching depending on the local flowfield motion. Despite the positive values of $\overline{v'^2}$ seen in Figs. 4 and 5, entrainment of freestream fluid downward into the jet is quite common. It is additionally clear that vortical activity can be

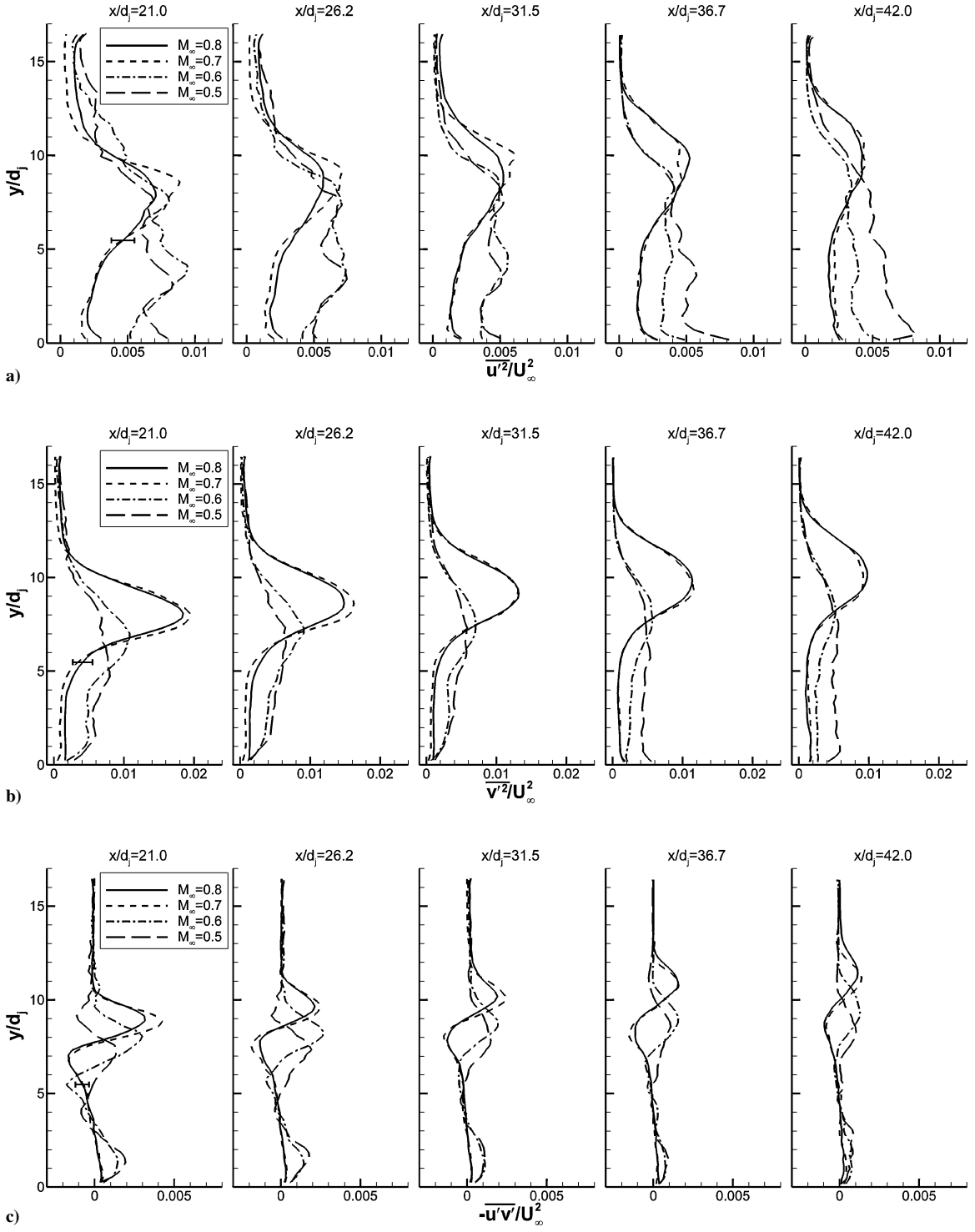

Fig. 5 Turbulent stress data extracted from vector fields at five locations downstream of the jet nozzle centerline for varying values of M_∞ while $J = 10.2$: a) streamwise turbulent stress, b) vertical turbulent stress, and c) turbulent shear stress.

found in the jet's wake as well as the mixing layer, possibly produced by the wake vortices as sketched in Fig. 1; this is most evident near the right-hand edge of Fig. 7a. However, the wake is, overall, much more quiescent than the jet itself, and coherent structures found within the wake often display a more elongated character rather than the elliptical shape typical of the jet eddies. Similar results are observed for all other flowfield cases except $M_\infty = 0.6$ and 0.5.

The instantaneous structure of the interaction for the $M_\infty = 0.5$ case is shown in the sample vector field of Fig. 7b. In contrast to the preceding case, eddies can be found from the jet all of the way to the wall, whereas for $M_\infty = 0.8$ such structures were found only in the jet itself. This inability to distinguish between the jet and its wake is typical of the $M_\infty = 0.6$ and 0.5 cases in comparison with the other five cases and provides further evidence that the flow behaves fundamentally differently for these two cases. Despite this variant behavior, however, the normalized vorticity strength of the eddies has a magnitude similar to that of Fig. 7a.

Mean Eddy Size

The ability of PIV to provide full-field instantaneous velocity realizations such as those shown in Fig. 7 enables a characterization of the typical eddy size to complement the traditional statistical approach to turbulence inherent in Figs. 4–6. To determine the mean large-scale eddy size, instantaneous velocity fluctuation

vector fields were ensemble averaged to produce a representative large-scale eddy. This was accomplished by first dividing the combined imaging region (upstream and downstream locations) into six vertical strips $4.2\,d_j$ wide and spanning the full height of the images, with each strip overlapping its neighbors by $0.8\,d_j$. In each of these strips, the position of maximum vorticity was located to mark the center of the strongest eddy in the strip, then this eddy was shifted to the mean position of these eddies over the entire data set. That is, the representative eddy found in each vertical strip was repositioned such that their centers coincided at their mean center point. Once colocated, the vector fields were averaged to produce a representative large-scale eddy whose minimum spatial extent is established by the spatial resolution of the PIV (approximately $0.5\,d_j$). This procedure was performed independently for eddies of positive and negative vorticity, in each of the six strips, for each of the seven flowfield cases.

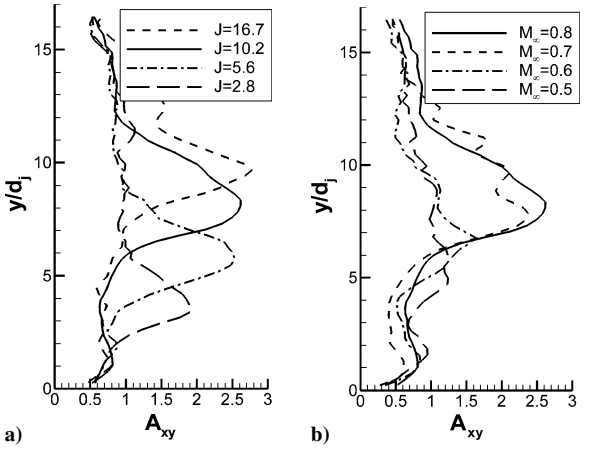

Fig. 6 Anisotropy coefficient ($\overline{v'^2}/\overline{u'^2}$) at $x/d_j = 21.0$: a) varying J while $M_\infty = 0.8$ and b) varying M_∞ while $J = 10.2$.

Figure 8 displays the resulting mean eddies of positive vorticity for the case where $J = 10.2$ and $M_\infty = 0.8$. Note that each of the six vortices was computed independently in its own vertical strip and is shown on the same plot only for convenience. As would be expected, the position of the eddies approximately tracks the penetration of the jet into the crossflow as it progresses downstream. The characteristic size of each representative eddy was determined by choosing its perimeter as the locus at which the vorticity is 10% of the maximum vorticity of that particular structure. The selection of 10% as the threshold is somewhat arbitrary, as it was chosen not for any physical significance but because it provided a boundary in excess of the background noise in the vorticity field for all seven cases (which is notably larger for the weaker jet cases, such as $J = 2.8$ or $M_\infty = 0.5$). The area of the eddy was calculated from the resulting boundary, from which the diameter d_z was found assuming it to be circular. This value d_z represents the characteristic length of the large-scale turbulent eddies in the interaction whose vorticity is aligned with the z axis.

Figure 9 displays the variation of d_z with downstream distance for all seven flowfield cases and for both positive and negative

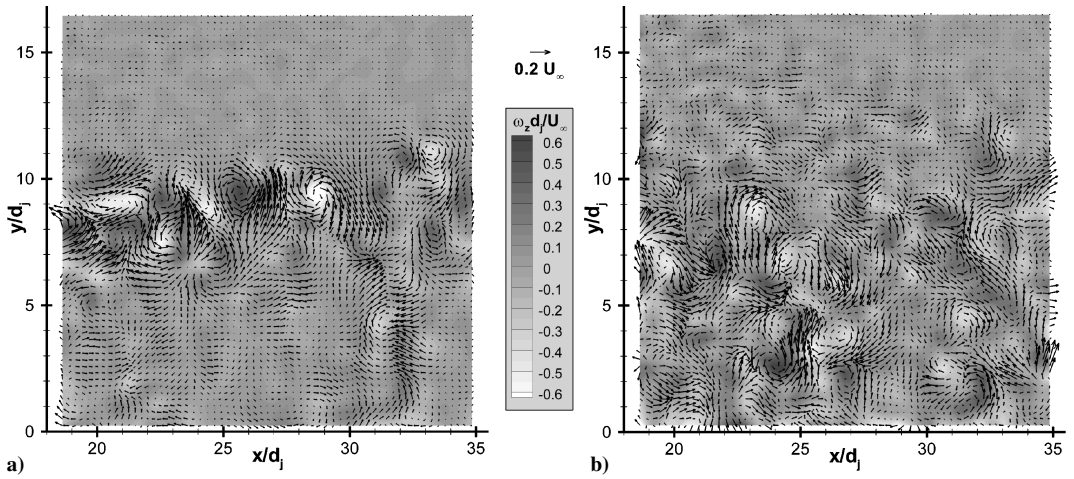

Fig. 7 Instantaneous realizations of the velocity fluctuation field overlaid on derived vorticity contours: a) $J = 10.2$ and $M_\infty = 0.8$; and b) $J = 10.2$ and $M_\infty = 0.5$.

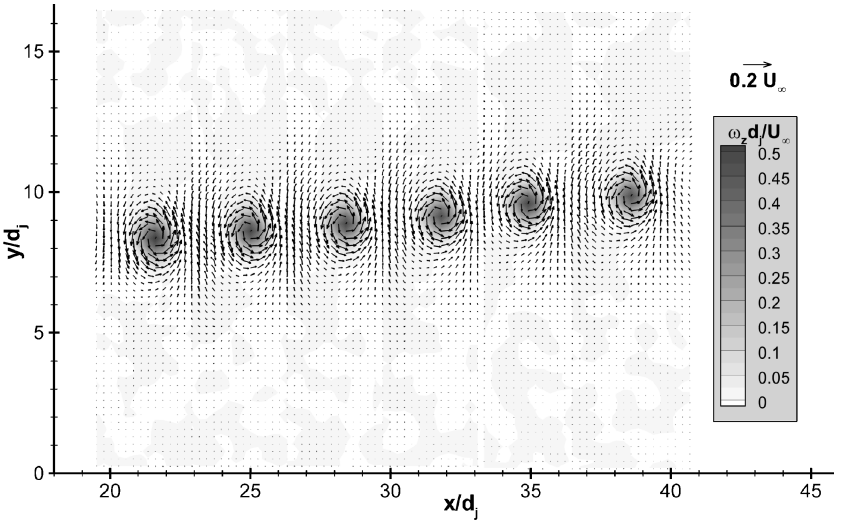

Fig. 8 Representative mean large-scale turbulent eddies of positive vorticity at six locations found by conditional ensemble averaging; $J = 10.2$ and $M_\infty = 0.8$.

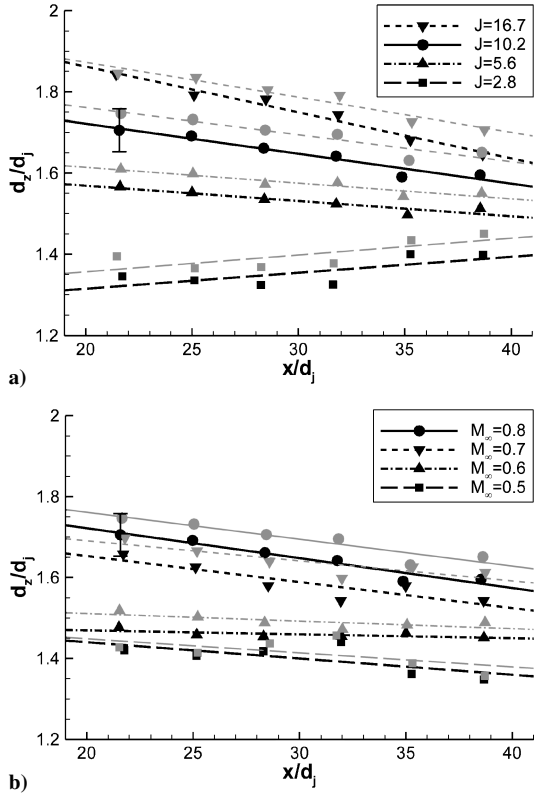

Fig. 9 Mean diameter d_z of the large-scale ensemble-averaged eddies whose vorticity is aligned in the z direction. Dark lines represent eddies of positive vorticity, whereas gray lines mark eddies of negative vorticity. Linear least-squares trendlines also are shown: a) varying J while $M_\infty = 0.8$ and b) varying M_∞ while $J = 10.2$.

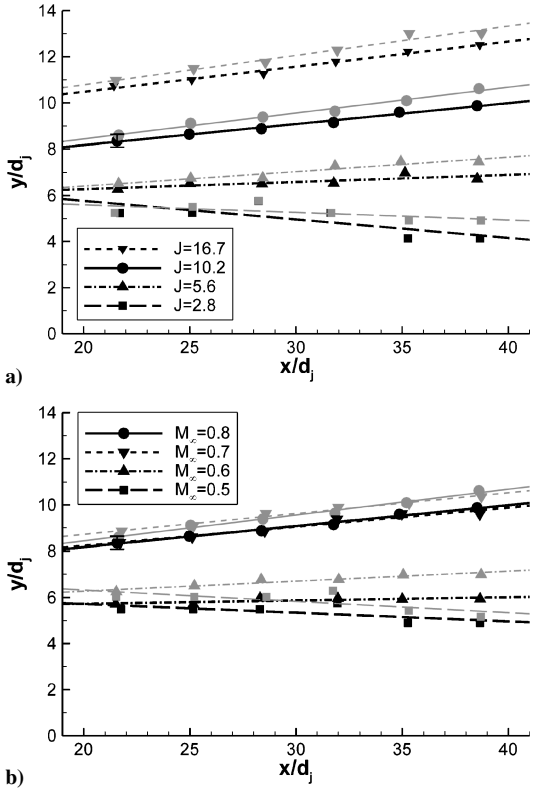

Fig. 10 Distance from the wall of the large-scale ensemble-averaged eddies whose vorticity is aligned in the z direction. Dark lines represent eddies of positive vorticity, whereas gray lines mark eddies of negative vorticity. Linear least-squares trendlines also are shown: a) varying J while $M_\infty = 0.8$ and b) varying M_∞ while $J = 10.2$.

vorticities. Linear fits to the measurements are shown; though the scatter in the points is too great to determine whether a linear fit is in fact accurate, they do serve well as trendlines. In all cases, eddies of negative vorticity are found to be larger than those of positive vorticity. Although this difference is approximately the same as the uncertainty of the measurement, the consistency of this observation over the entire data set suggests that it is authentic. It also is shown that the eddy size decreases with downstream distance in all cases except $J = 2.8$. However, the latter case might be an anomaly, as the first four points that originate from the upstream imaging region show a decrease in d_z, whereas the two points from the downstream imaging region are larger. Therefore, a mismatch between the two stations might be responsible for the rising trendline. Given that this case involves the weakest jet, the signal-to-noise ratio of the measurements is smallest and thus most prone to discrepancies. It also is evident in Fig. 9b that the measurements for $M_\infty = 0.8$ and 0.7 do not exhibit similarity, even though the mean data and turbulence quantities found earlier did collapse for these two cases.

Figure 10 shows the vertical position of the ensemble-averaged eddies. Here, it can be seen that just as eddies of negative vorticity were found to be larger than those of positive vorticity, they additionally are located somewhat farther from the wall. In most cases, the eddies move farther from the wall with increasing downstream distance. Exceptions to this are found for $J = 2.8$, where the measurements might be anomalous as just discussed, and for $M_\infty = 0.6$ and 0.5, where the flowfield structure already is known to be deviant.

To further examine the position of the large-scale structures, the location of each eddy was recorded prior to shifting its position for the ensemble averaging. These results are displayed in Fig. 11 as histograms of the vertical distance from the wall, which was found from the centroid location of each eddy, c_y. Independent histograms were generated for eddies of positive and negative vorticity and are overlaid in the figure. Two cases are shown, one for the $J = 10.2$ and $M_\infty = 0.8$ condition and one for $J = 10.2$ and $M_\infty = 0.5$, both at a downstream position of $x/d_j \approx 25$ (i.e., the second vertical strip). Other downstream positions produced similar results, save that they

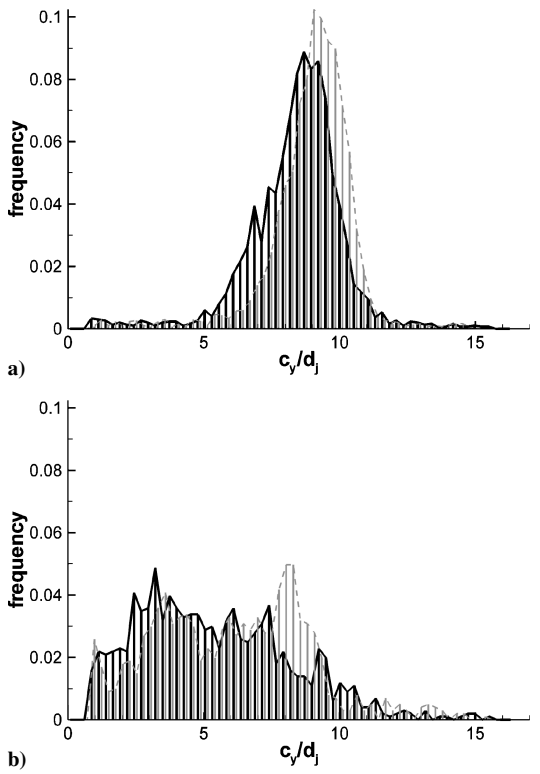

Fig. 11 Histograms of the vertical position of the strongest large-scale eddies at approximately $x/d_j \approx 25$. Dark lines show eddies of positive vorticity, and gray lines show those of negative vorticity: a) $J = 10.2$ and $M_\infty = 0.8$ and b) $J = 10.2$ and $M_\infty = 0.5$.

are stretched in the y direction to reflect the increasing penetration of the jet.

Figure 11a shows that the distribution of the eddy position is approximately Gaussian for $M_\infty = 0.8$, centered near the mean jet trajectory seen in Fig. 4. The distribution for eddies of negative vorticity is shifted slightly further from the wall as compared to that for eddies of positive vorticity, consistent with Fig. 10a. The histograms show that the strong large-scale eddies tend to be found within the jet and not its wake, as was the case in the instantaneous realization shown in Fig. 7a. In contrast, the distribution shown in Fig. 11b for $M_\infty = 0.5$ does not exhibit a Gaussian character, and eddies are found as commonly in the jet wake as in the jet itself. This observation is supportive of the instantaneous vector field of Fig. 7b, additionally demonstrating that the large-scale structures found closer to the wall are as probable as those in the jet itself to possess the maximum vorticity magnitude sought by the ensemble-averaging algorithm. The difference between eddies of positive and negative vorticity is not as readily discerned as in Fig. 11a, though the histogram suggests that eddies of negative vorticity are somewhat more likely to be seen further from the wall in comparison with those of positive vorticity. Note that the distributions in Fig. 11b are noisier than those in Fig. 11a because one-third as many PIV image pairs were collected.

The large-scale structure size alternatively can be determined using traditional statistical methods for treating turbulence length scales. The integral length scale is found by integrating the correlation function of one velocity at a fixed point in the interaction with the velocity at some variable distance. In the present case, the correlation function

$$R(y) = \frac{\overline{v_1' v_2'}}{\sqrt{\overline{v_1'^2}}\sqrt{\overline{v_2'^2}}}$$

is computed based on v_1' fixed at the nominal centerline of the jet with v_2' varied along a vertical line from the wall to the edge of the imaging region. The choice of v' over u' and the constant position of the jet centerline were selected because they were found to yield the smoothest, most useful correlation curves. $R(y)$ was calculated at each downstream station, from whose integration the length scale L_z was found.

The resulting profiles of L_z are shown in Fig. 12. As in the profiles of d_z in Fig. 9, linear curve fits are overlaid to serve as trendlines, though the data uncertainty is too large to determine if the behavior is linear. The true values of L_z for $J = 16.7$ probably are larger than found here; the penetration of this strong jet places it in proximity to the edge of the imaging region, which truncates the correlation curves and therefore reduces L_z. The discontinuity between the upstream and downstream imaging regions for $J = 2.8$ that was observed in Fig. 9a also is present in Fig. 12a. Despite these limitations, however, it is evident that values of L_z are roughly twice those of d_z. This is not greatly surprising because the two length scales are determined in such different fashions even if both purportedly represent large-scale turbulent structures. Of more substantial concern is that in all cases L_z increases with downstream distance, whereas in Fig. 9 d_z was shown to generally decrease with downstream distance.

The different behavior of L_z as compared to d_z might occur because the ensemble averaging includes smaller eddies to which the correlation curves are less susceptible. Small structures (but still large scale from a turbulence perspective, given the spatial resolution of the PIV data) that possess the maximum or minimum vorticity in an ensemble-average region will be included in the mean eddy calculation in equal weight with larger structures. However, the velocity fluctuations associated with a smaller structure will be correlated over a shorter distance than those from a larger structure and hence will have a reduced impact upon the correlation curve. Essentially, the correlation function acts as a low-pass filter in comparison with the ensemble average. A similar effect was found in PIV measurements by Olsen[26] when comparing ensemble-averaged mixing-layer structures with those found by linear stochastic estimation from spatial correlations, and the observations of Adrian et al.[27] support the discovery of different physical structures dependent upon how PIV vector fields are treated.

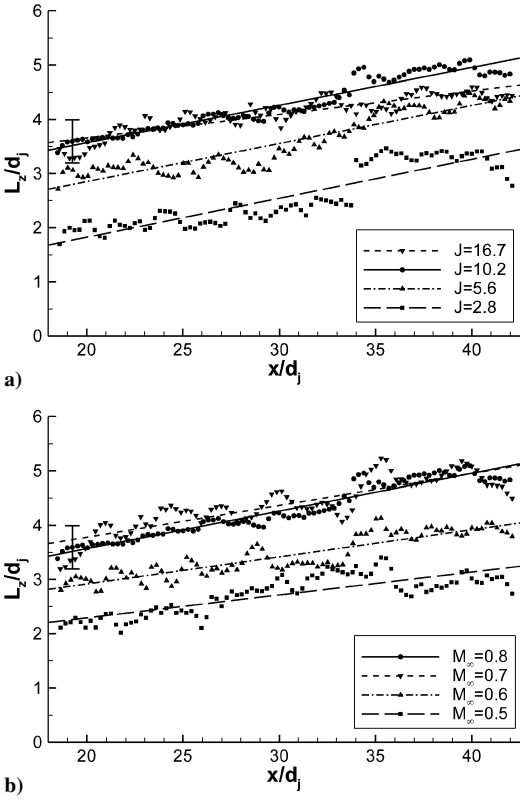

Fig. 12 Integral turbulent length scale derived from the correlation function of v' in the vertical direction. Linear least-squares trendlines also are shown: a) varying J while $M_\infty = 0.8$ and b) varying M_∞ while $J = 10.2$.

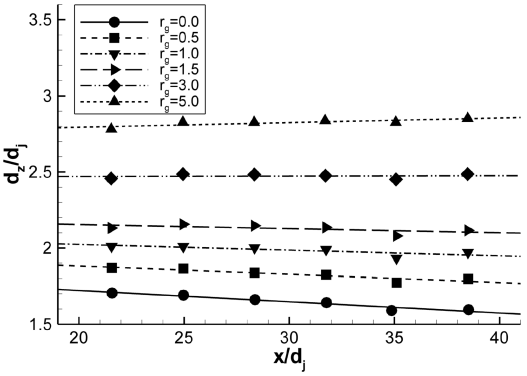

Fig. 13 Mean diameter of the large-scale ensemble-averaged eddies of positive vorticity for varied degrees of low-pass filtering: $J = 10.2$ and $M_\infty = 0.8$.

To test this hypothesis, the PIV vector fields were low-pass filtered at different cutoff levels prior to ensemble averaging, then the alteration in the calculated eddy diameter was examined. This was done only for the case where $J = 10.2$ and $M_\infty = 0.8$ for eddies of positive vorticity. The low-pass filtering was accomplished using a Gaussian kernel whose radius r_g was varied to achieve different filter strengths. Figure 13 displays the results, which show that as r_g increases, the magnitude of d_z rises nearer to comparable values of L_z and the slope of its trendline with downstream distance becomes milder, eventually shifting to a positive value. The latter effect indicates that low-pass filtering does influence the downstream trend of d_z and, given sufficient filter strength, produces that found in L_z. This suggests that the measurements of d_z and L_z are both accurate, but d_z incorporates a wider range of structure sizes (whose lower limit is dictated by the PIV spatial resolution) than L_z, accounting for the differing behavior. The magnitude and downstream trend of L_z is comparable to that of the width of the mean vertical velocity profiles from Ref. 23, which is representative of the extent of the counter-rotating vortex pair. Therefore, L_z corresponds to the size

of the vortex pair, whereas d_z can be interpreted as a measure of the instantaneous large-scale turbulent eddies that comprise it; while the vortex pair expands with downstream distance, its constituent instantaneous structures tend to become smaller.

Summary

Particle-image-velocimetry data have been acquired in the centerline streamwise plane of the far field of the interaction generated by an overexpanded axisymmetric supersonic jet exhausting transversely from a flat plate into a subsonic compressible crossflow. Seven sets of flowfield conditions were studied that varied the jet-to-freestream dynamic pressure ratio J and the crossflow Mach number M_∞. Whereas a previous work examined these data based upon their mean velocity characteristics,[23] the present document concerns the turbulent properties derived from the fluctuating velocity measurements.

Turbulent stresses were found by subtracting the mean velocity field for each case from each individual vector field to yield the velocity fluctuations, then statistically computing the three components of the stress tensor available from the two-dimensional measurements. These data show that the magnitudes of $\overline{u'^2}/U_\infty^2$, $\overline{v'^2}/U_\infty^2$, and $-\overline{u'v'}/U_\infty^2$ all increase with larger J while M_∞ remains constant and that the vertical position of their peaks lies further from the wall for larger J. These turbulent stress magnitudes diminish with downstream distance while their vertical position increases. The vertical position of the peaks in $\overline{u'^2}/U_\infty^2$ and $\overline{v'^2}/U_\infty^2$ and the inflection point in $-\overline{u'v'}/U_\infty^2$ all coincide with the position of the peak mean streamwise velocity deficit. Similarity is observed in the turbulent stresses for $M_\infty = 0.8$ and 0.7 when J remains constant, but not for $M_\infty = 0.6$ and 0.5; this was observed in the mean data as well.[23] These latter two cases also exhibit two inflection points in their $-\overline{u'v'}/U_\infty^2$ profiles and possess lower anisotropy than the other cases.

Instantaneous realizations of the velocity fluctuation fields show that large-scale turbulent eddies of both positive and negative vorticity are present in the jet with weaker coherent structures found in the wake. This is true for all cases studied except for $M_\infty = 0.6$ and 0.5, where such structures are present all of the way to the wall with no distinction between the jet and its wake. Histograms of the vertical location of these eddies support this observation. Representative eddies were calculated by ensemble averaging the instantaneous velocity fluctuation fields centered on the peak vorticity, from which it was shown that eddies with vorticity of negative sign tend to be slightly larger and lie farther from the wall than those of positive sign. The characteristic length scale of these eddies was calculated as their mean diameter, showing that eddies tend to be larger for greater values of J and tend to diminish in size with downstream distance. The deviant cases of $M_\infty = 0.6$ and 0.5 do not necessarily adhere to these trends. The integral turbulent length scale was found from profiles of the correlation coefficient of the vertical velocity fluctuation v'. This length scale is approximately twice that found from the ensemble averages and shows an increasing trend with downstream distance. The discrepancy between these two length scales occurs because the integral length scale essentially acts as a low-pass filter on the velocity field, whereas the ensemble-average process is limited only by the spatial resolution of the velocity measurements. Confirmation of this was found by low-pass filtering the velocity fluctuation fields prior to ensemble averaging, which increased the calculated length scale and produced a trend of increasing structure size with downstream distance.

Acknowledgments

This work is supported by Sandia National Laboratories and the U.S. Department of Energy. Sandia is a multiprogram laboratory operated by Sandia Corporation, a Lockheed Martin Company, for the U.S. Department of Energy's National Nuclear Security Administration under Contract DE-AC04-94AL85000. The authors thank the following Sandia National Laboratories staff members for their insightful advice and discussions: F. G. Blottner, S. P. Kearney, W. L. Oberkampf, J. L. Payne, C. W. Peterson, M. R. Prairie, and W. P. Wolfe.

References

[1]Cassel, L. A., Durando, N. A., Bullard, C. W., and Kelso, J. M., "Jet Interaction Control Effectiveness for Subsonic and Supersonic Flight," U.S. Army Missile Command, Rept. RD-TR-69-21, Redstone Arsenal, AL, Sept. 1969.

[2]Dormieux, M., and Marsaa-Poey, R., "Numerical Assessment of Aerodynamic Interactions on Missiles with Transverse Jets Control," *Computational and Experimental Assessment of Jets in Cross Flow*, AGARD CP 534, 1993, pp. 30.1–30.11.

[3]Cassel, L. A., "Applying Jet Interaction Technology," *Journal of Spacecraft and Rockets*, Vol. 40, No. 4, 2003, pp. 523–537.

[4]Srivastava, B., "Aerodynamic Performance of Supersonic Missile Body- and Wing Tip-Mounted Lateral Jets," *Journal of Spacecraft and Rockets*, Vol. 35, No. 3, 1998, pp. 278–286.

[5]Brandeis, J., and Gill, J., "Experimental Investigation of Super- and Hypersonic Jet Interaction on Missile Configurations," *Journal of Spacecraft and Rockets*, Vol. 35, No. 3, 1998, pp. 296–302.

[6]Graham, M. J., Weinacht, P., and Brandeis, J., "Numerical Investigation of Supersonic Jet Interaction for Finned Bodies," *Journal of Spacecraft and Rockets*, Vol. 39, No. 3, 2002, pp. 376–383.

[7]Margason, R. J., "Fifty Years of Jet in Cross Flow Research," *Computational and Experimental Assessment of Jets in Cross Flow*, AGARD CP 534, 1993, pp. 1.1–1.41.

[8]Fric, T. F., and Roshko, A., "Vortical Structure in the Wake of a Transverse Jet," *Journal of Fluid Mechanics*, Vol. 279, 1994, pp. 1–47.

[9]Krothapalli, A., Lourenco, L., and Buchlin, J. M., "Separated Flow Upstream of a Jet in a Crossflow," *AIAA Journal*, Vol. 28, No. 3, 1990, pp. 414–420.

[10]Kelso, R. M., and Smits, A. J., "Horseshoe Vortex Systems Resulting from the Interaction Between a Laminar Boundary Layer and a Transverse Jet," *Physics of Fluids*, Vol. 7, No. 1, 1995, pp. 153–158.

[11]Kelso, R. M., Lim, T. T., and Perry, A. E., "An Experimental Study of Round Jets in Cross-Flow," *Journal of Fluid Mechanics*, Vol. 306, 1996, pp. 111–144.

[12]Sykes, R. I., Lewellen, W. S., and Parker, S. F., "On the Vorticity Dynamics of a Turbulent Jet in a Crossflow," *Journal of Fluid Mechanics*, Vol. 168, 1986, pp. 393–413.

[13]Yuan, L. L., Street, R. L., and Ferziger, J. H., "Large-Eddy Simulations of a Round Jet in Crossflow," *Journal of Fluid Mechanics*, Vol. 379, 1999, pp. 71–104.

[14]Gruber, M. R., Nejad, A. S., Chen, T. H., and Dutton, J. C., "Mixing and Penetration Studies of Sonic Jets in a Mach 2 Freestream," *Journal of Propulsion and Power*, Vol. 11, No. 2, 1995, pp. 315–323.

[15]VanLerberghe, W. M., Santiago, J. G., Dutton, J. C., and Lucht, R. P., "Mixing of a Sonic Transverse Jet Injected into a Supersonic Flow," *AIAA Journal*, Vol. 38, No. 3, 2000, pp. 470–479.

[16]McCann, G. J., and Bowersox, R. D. W., "Experimental Investigation of Supersonic Gaseous Injection into a Supersonic Freestream," *AIAA Journal*, Vol. 34, No. 2, 1996, pp. 317–323.

[17]Bowersox, R. D. W., "Turbulent Flow Structure Characterization of Angled Injection into a Supersonic Crossflow," *Journal of Spacecraft and Rockets*, Vol. 34, No. 2, 1997, pp. 205–213.

[18]Santiago, J. G., and Dutton, J. C., "Velocity Measurements of a Jet Injected into a Supersonic Crossflow," *Journal of Propulsion and Power*, Vol. 13, No. 2, 1997, pp. 264–273.

[19]Orth, R. C., and Funk, J. A., "An Experimental and Comparative Study of Jet Penetration in Supersonic Flow," *Journal of Spacecraft and Rockets*, Vol. 4, No. 9, 1967, pp. 1236–1242.

[20]Kamotani, Y., and Greber, I., "Experiments on a Turbulent Jet in a Cross Flow," *AIAA Journal*, Vol. 10, No. 11, 1972, pp. 1425–1429.

[21]Papamoschou, D., and Hubbard, D. G., "Visual Observations of Supersonic Transverse Jets," *Experiments in Fluids*, Vol. 14, No. 6, 1993, pp. 468–471.

[22]Keffer, J. F., and Baines, W. D., "The Round Turbulent Jet in a Cross-Wind," *Journal of Fluid Mechanics*, Vol. 15, 1963, pp. 481–496.

[23]Beresh, S. J., Henfling, J. F., Erven, R. J., and Spillers, R. W., "Penetration of a Transverse Supersonic Jet into a Subsonic Compressible Crossflow," *AIAA Journal*, Vol. 43, No. 2, 2005, pp. 379–389.

[24]Samimy, M., and Lele, S. K., "Motion of Particles with Inertia in a Compressible Free Shear Layer," *Physics of Fluids A*, Vol. 3, No. 8, 1991, pp. 1915–1923.

[25]Melling, A., "Tracer Particles and Seeding for Particle Image Velocimetry," *Measurement Science and Technology*, Vol. 8, No. 12, 1997, pp. 1406–1416.

[26]Olsen, M. G., "Planar Velocity Measurements in an Incompressible and a Weakly Compressible Mixing Layer," Ph.D. Dissertation, Dept. of Mechanical and Industrial Engineering, Univ. of Illinois, Urbana, IL, 1999.

[27]Adrian, R. J., Christensen, K. T., and Liu, Z.-C., "Analysis and Interpretation of Instantaneous Turbulent Velocity Fields," *Experiments in Fluids*, Vol. 29, No. 3, 2000, pp. 275–290.

M. Sichel
Associate Editor